Characterization of atherosclerotic plaque: a contrast-detail study using multidetector and cone-beam computed tomography

Nima Kasraie,[1] Peter Mah,[2] Carl R. Keener,[1,3] Geoffrey D. Clarke[1a]
Department of Radiology[1] and Department of Comprehensive Dentistry,[2] The University of Texas Health Science Center at San Antonio, San Antonio, TX; Medical and Radiation Physics Incorporated,[3] San Antonio, Texas, USA
clarkeg@uthscsa.edu

A Hindmarsh-Rose model perceptibility phantom containing inserts with various *in vitro* atherosclerotic plaque compositions was constructed and imaged on a clinical 64 slice multidetector (MDCT) system using 80 and 120 kVp settings and two other cone-beam (CBCT) systems at 80 kVp. Perceptibility of the simulated lipid-fibrotic plaque solutions in the images was evaluated by six observers. The effective doses of the protocols employed were estimated using phantom CTDI-vol measurements placed at identical settings. The CBCT system allowed reduction in effective dose in comparison with the conventional MDCT system for imaging of the carotid plaque phantoms without degrading image quality. The CBCT dose was less than MDCT, with a mean dose of 1.14 ± 0.01 mSv and 1.11 ± 0.02 mSv for MDCT using two measuring techniques vs. 0.35 ± 0.01 mSv for CBCT. The image quality analysis showed no significant differences in the contrast-detail (C-D) curves of the best performing CBCT vs. clinical MDCT ($p > 0.05$) using a Mann-Whitney U test. Results indicate that low-tube–potential CBCT may produce comparable C-D resolution for phantom-based representations of soft plaque types with respect to MDCT systems. This study suggests that the utility of low kVp CT techniques for evaluating carotid vulnerable atherosclerotic plaque merits further study.

I. INTRODUCTION

The current clinical diagnostic methods for detecting vulnerable atherosclerotic plaque are largely based on stenosis angiography and intravascular ultrasound (IVUS).[1,2] These approaches have limitations, and neither has the ability to differentiate soft plaque (fibrotic vs. fatty plaque), which are rupture-prone and known to induce plaque instability. Plaque composition, rather than the degree of arterial stenosis, is thought to be the critical determinant of both risk of rupture and subsequent thrombogenicity.[3] An imaging technique capable of noninvasively quantifying atherosclerotic plaque composition in addition to stenosis would likely be useful for detecting early atherosclerotic disease and improving the current understanding of the pathogenesis of atherosclerosis.

Soft plaque lesions are inherently low-contrast in nature, making their detection an essential aim in diagnostic imaging. Test phantoms with low-contrast details can be used[4] for the purposes of quantitative evaluation of low-contrast detail perceptibility. Several possible measurement methods have been described in the literature. However, to date there have been few

---

a   Corresponding author: Geoffrey D. Clarke, Department of Radiology, The University of Texas Health Science Center at San Antonio, 7703 Floyd Curl Drive, San Antonio Texas, USA; phone: 210-567-1361; fax: 210-567-5541; email: clarkeg@uthscsa.edu

studies examining plaque characterization using these phantoms. Most plaque imaging studies are either *in vivo*, animal, or endarterectomy *ex vivo*. These approaches all have limitations in their abilities to fully characterize vulnerable plaque including long scan times, high radiation dose loads (which eliminate longitudinal studies), and animal plaque deviation. Furthermore, costly and prolonged clinical trials are often required for validating a new or alternative imaging technique intended for clinical use, especially when more established methods already exist.[5] Phantoms can help circumvent these difficulties by offering a different type of model, which has the additional ability to better control the experimental design.

The flexibility in designing experiments that phantoms offer can be employed to demonstrate the application of computed tomography for differentiation of lipid-rich and fibrotic plaque. A Hindmarsh-Rose model-based lesion composition phantom may be used to test the contrast relationships between fatty, fibrotic, and calcified components of vulnerable plaque, and compare the results between two competing modalities. A C-D technique using such phantoms can address the limits of imaging performance in a systematic manner, and is especially advantageous for modality system assessments by comparing multiple curves. One curve can be produced from each technique (different imaging systems, or same system under different operating conditions), and then compared to another.[6]

The aim of this study was to develop a suitable lesion composition phantom and to evaluate the application of computed tomography for differentiation of *in vitro* lipid-rich vs. fibrotic plaque samples at clinical interscanner protocols of 120 kVp and 80 kVp. The phantom was used to characterize simulated atherosclerotic plaques by comparison of the C-D characteristics of conventional MDCT and clinical low-tube–potential CBCT images, based on Hindmarsh-Rose model predictions.

II.   MATERIALS AND METHODS

A.   The phantom

C-D phantoms (also known as Hindmarsh-Rose model phantoms) have been used as test objects and analysis tools in various diagnostic imaging modalities.[6-10] These perceptibility phantoms are quantitative tools with designs that take into account the physics of attenuating transmission beams. That is to say they generate a range of image contrasts determined by phantom thickness (e.g., cavity hole depth or water column height). In the current study, a phantom was designed and constructed in which contrast depends, not on the traditional attenuating properties of the phantom (i.e., hole thickness or water column height), but on its differing contents such as varying plaque composition mixture. This approach enables a comparison of the low-contrast performance of different scanners.

The lesion composition phantom was designed to assess the visible detectability of vulnerable atherosclerotic plaque in this study. The design was performed and evaluated using formZ CAD software (AutoDesSys, Columbus OH) and the phantom was constructed of cast acrylic block (McMaster-Carr, Elmhurst, IL) with a mean CT attenuation value approximating typical fibrotic atherosclerotic tissue. A total of 27 cylindrical inserts (9 rows × 3 inserts) of 0.4, 0.6, 0.8, 1.0, 1.5, 2.0, 2.5, 3.0, and 3.5 mm in diameter and a reference cavity of 12 mm were drilled perpendicularly into the plastic block, as shown in Fig. 1. The dimensions of each disk was 50.8 mm in diameter and 12.7 mm in thickness, with total volume allocated for injecting plaque in each phantom at 1068.77 mm^3 per composition. There were five phantom segments (for five different compositions) overall, connected via a stabilizing shaft (Fig. 2) to prevent rotation while submerged in a scattering medium such as water.

The sizes of the phantom cavities were chosen with the resolution limits of conventional CT systems in mind and in accordance with published data from subjects with acute atherosclerotic arterial events, whose typical lipid core dimensions range from 1–5 mm^2, with the consideration that at least 80% of plaques have core areas exceeding 1.0 mm^2.[11,12]
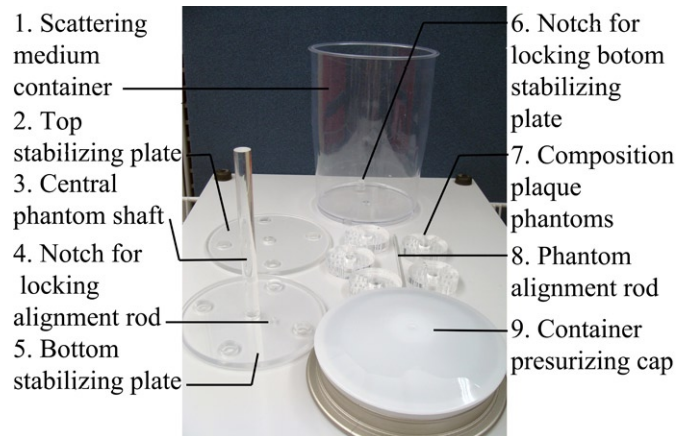
FIG. 1. The phantom consisted of five plastic cylinders with holes containing the simulated plaques, which were positioned on a coaxial support rod and housed in a water-filled container. In this view, the phantom structure was disassembled into its constituent parts.
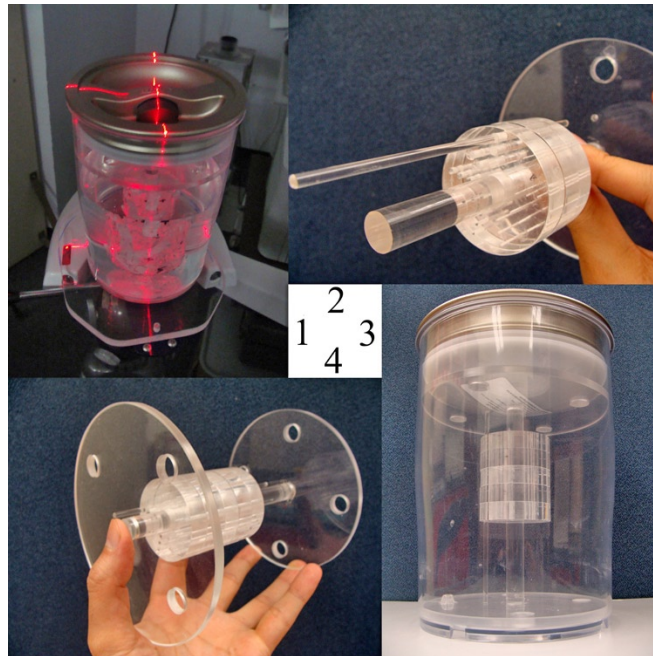

FIG. 2. View of plaque composition phantom assembly: (1) phantom assembly positioned for scanning; (2) disassembled to reveal how central phantom shaft and alignment rod support cylindrical phantom inserts; (3) phantom structure assembled without water; (4) support structure with both ends on.

B. Plaque lesion composition

Emulsions with varying concentrations of lipid and fiber were injected into the phantoms to simulate regions of atherosclerotic lipid core and surrounding fibrotic tissue, with each varying composition emulsified within a 2 mL solution of 5% acetic acid and ethanol, in varying proportions of lipid and fiber, to produce different lesion compositions consisting of five lesion compositions of lipid-fiber with mass ratios of 82:18, 71:29, 60:40, 49:51, and 37:63, respectively, all totaling 100 mgr each.

The lipid solution used was a by-weight composition of 25% free cholesterol (Product Number C8503, Sigma-Aldrich, St. Louis, MI), 19% cholesteryl palmitate (Product Number C6072, Sigma-Aldrich), 36% cholesteryl oleate and 20% triglycerid, as per the distribution values reported by McArthur[13] for atheroma in human lesions. The corresponding fibrotic solution was 20% elastin (Product Number E1625, Sigma-Aldrich) and 80% Type I Collagen (BD Biosciences, Bedford MA), as per reported values for fibrotic plaque content in human atherosclerosis lesions.[14-16] Each composition occupied a total of 1.07 mL of the 27 inserts in each phantom.

C.   Imaging protocols and settings

The MDCT protocol used was that of a clinically used 64 slice Angio Neck (Brilliance 64, Philips Medical Systems, Cleveland, OH) at 80 kVp and 120 kVp for all lesions, followed by two different cone-beam fixed geometry (rotating gantry) clinical CBCT units (Morita 3D Accuitomo 80 XYZ Slice View Tomograph, J. Morita MFG. Corp., Kyoto, Japan) and (Planmeca Promax 3D, Planmeca USA, Roselle, IL).

The phantoms were positioned at isocenter and oriented parallel to the axis of the gantry so that they would be exposed radially inward (Fig. 2). Table 1 summarizes the protocols used for scanning the plaque phantom.

TABLE 1. Scan protocols.

	Philips Brilliance	*Planmeca Promax 3D*	*Morita 3D Accuitomo*
kVp	80/120	80	80
Filter	Standard	---	---
Collimation	64×0.625	---	---
Pitch	1.2	---	---
Rotation Time	0.75 sec	---	17 sec
DFOV	80 mm	80 mm	80 mm
Matrix	512	250	507
Thickness	1.0	---	1.28[a]
Exposure Time	0.624 sec	12.25 sec	17 sec
mA	321	14	10
X-Y res.	0.4 mm	0.32 mm	0.16 mm

[a] Postacquisition processing when exporting into DICOM.

D.   Dose measurements

Six optically stimulated luminescence (OSL) detectors (Landauer, Glenwood, IL; serial# DN093015717) with sensitivity of 0.93 were placed on the phantom at 90° interval pairs during measurements in each of the MDCT 120 kVp and CBCT 80 kVp scans, and were then read 6 hours postexposure by an InLight microStar Reader (Landauer). These measurements provided a crude estimate for comparing the relative dose of the two imaging techniques. Another, more quantitative assessment used, was the measurement of the CTDI-vol of both modalities using an adult head 100 mm pencil chamber phantom composed of polymethyl methacrylate (PMMA), as per ACR guidelines. In this protocol the CTDI dose was measured in the CTDI phantom at the isocenter and at the 12-o'clock position in the periphery, three times each. Values of CTDI-vol were then calculated, as per the definitions of two published standards: IEC60601-2-44[17] and ICRP87.[18] This procedure allowed effective dose calculations based on the anatomy of the neck area. The detectors used were an Unfors Xi 1 (Unfors RaySafe AB, Billdal, Sweden), and Triad 3 Electrometer model 35050A (Keithley Instruments, Inc., Cleveland, OH).

Effective dose provides a method for comparing biological effects of radiation between diagnostic procedures of different types. A reasonable estimate, independent of scanner type, was obtained by employing the proper weighting factor, k, which is only dependent on the body region being exposed:[19]

$$\text{Effective Dose} = k \times DLP \tag{1}$$

where k is the weighting factor in mSv.mGy^{-1}.cm^{-1}, and DLP is the dose length product in mGy.cm. The weighting factor used in this study to estimate the effective dose was 0.0059 mSv.mGy^{-1}.cm^{-1} for the neck region, as per the values reported in AAPM Report 96.[20]

To attain a comparison between the measured beams, the half-value layer (HVL) of the Philips and Morita units were measured at their respective isocenters, using an Unfors Solo (Unfors RaySafe AB) detector. The measurement setup for measuring HVL (right) and CTDI (left) in the Morita unit is shown in Fig. 3.

FIG. 3. Setup for measuring HVL at isocenter for the Morita 3D Accuitomo cone-beam CT unit using an Unfors dosimeter (right), and CTDI on same cone-beam unit (left).

E. Effective energy

The effective energies were determined using an eight-material reference phantom (Fig. 4) with known physical properties, as previously described by Mah et al.[21] The mass attenuation coefficients used were derived from National Institute of Standards and Technology (NIST) Tables of X-ray Mass Attenuation Coefficients and Mass Energy Absorption Coefficients from 1 keV to 20 MeV for elements Z = 1 to 92 (NISTIR 5632 Version) from JH Hubbell and SM Seltzer in the Ionizing Radiation Division of the Physics Laboratory National Institute of Standards and Technology in Gaithersburg, MD, USA.

The eight-material phantom was scanned using clinical protocol of 80 kVp and 7 mA on the Morita Accuitomo 80 and 80 kVp and 12 mA on the Planmeca ProMax 3D. The CBCT data were then exported as a raw DICOM dataset and transferred to Cybermed's On Demand 3D software (Cybermed Inc., Irvine, CA) for analysis. The average gray levels for seven of the eight standard materials were determined and fitted against the linear attenuation coefficients for the respective reference materials at various photon energies using a regression analysis. The energy resulting in the best linear fit or an R value closest to one was selected as the "effective energy" of the beam. The gray levels for air were not utilized in the regression analysis as it
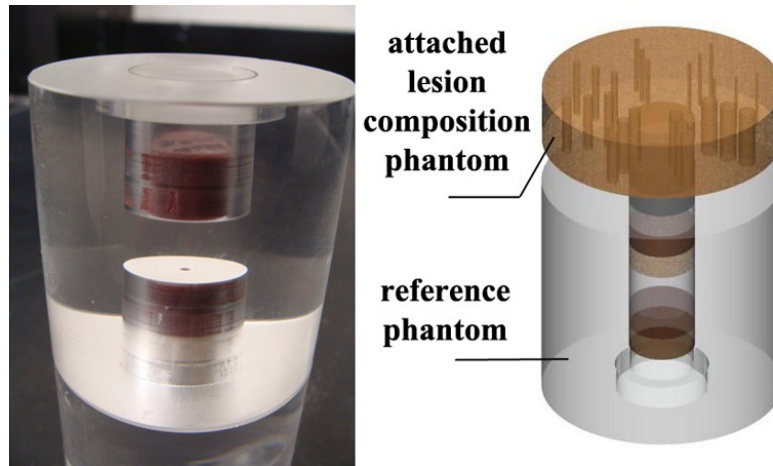
FIG. 4. A photograph of the reference phantom used for measuring effective energy of modalities is shown (left). The diagram depicts how a phantom can be attached to one or multiple lesion composition phantoms (right).

appeared that the gray levels on some CBCT devices are artificially set to register at -1000 or very close to it.

In a previous paper, Mah et al.[21] reported that the average gray levels were linearly related to the Hounsfield units of each material, as given by the equation:

$$HU = (\mu_{material} - \mu_{water})/(\mu_{water}) \times 1000 \tag{2}$$

Hence the gray levels could be plotted against the linear attenuation coefficients of each material to establish an effective energy.

F.   Analytical methods

Six independent observers (three diagnostic imaging physicists, two clinical radiologists, and one optometrist) evaluated visibility thresholds of the phantoms without prior knowledge of the phantom characteristics and blinded to the results. The MDCT and CBCT images were marked and ordered into stacks of cross-sectional images, and displayed with fixed level/window settings through all observations, for a total of 240 images. These images were presented in random order to the readers who were asked to identify the smallest size, of which all three cavities were simultaneously visible, per each composition, excluding bubbles, and allowing frame toggling. Internal noise was minimized[7,22] by using ambient light levels and fixed conditions. An observation distance of 50 cm was maintained throughout, with small variations in observation distance allowed, as no major impact in observer response was to be expected.[7,23] The boundary of the detected cavity was then delineated with an ROI marker tool in order to correctly measure the CT number S_i of the ith simulated lesion. The definition[24] used to compute the corresponding CNR was:

$$CNR_i = \frac{|S_i - S_b|}{\sqrt{\sigma_i^2 + \sigma_b^2}} \tag{3}$$

where S_b is the average of the corresponding measured background signal of the image pixel values for that specific ith ROI, with σ denoting the standard deviation. This value was assigned to the ordinate[25] of the C-D curve, with a similar procedure performed for each C-D data point extracted.

The accumulated data were then exported and a nonlinear regression computation was performed using Mathematica 6.0 (Wolfram Research Inc., Champaign, IL). The Hindmarsh-Rose model equation used to fit the data was a customized derivation[26] of the form,

$$C = \frac{k}{d - d_0} \qquad (4)$$

where d_0 is the resolution limit of the system, k is the fitting parameter, d is the abscissa variable (insert size), and C is the contrast relative to background. The Mathematica program computed the fitting parameter, k, by using the Levenberg-Marquardt method for nonlinear least-squares, which finds numerical values of the parameter k that enable the customized Hindmarsh-Rose model equation[4] to yield a best fit to the CNR values as a function of the observed phantom detail.

Differences between the resulting C-D curves were tested for significance using nonparametric statistics. The two-tailed Mann-Whitney U test was used for pair comparisons, while the Kruskal-Wallis H test was used for an overall group comparison. Critical values representing a probability, $p \leq 0.05$, were considered adequate for rejecting the null hypothesis. Calculations were performed using a computational statistics package (PASW Statistics 18 for Windows, IBM, Armonk, NY).

The inverse image quality figure, denoted IQF_{inv}, was then used as a further quantitative comparison tool for evaluating the C-D phantom images. The IQF_{inv}, a measure for the ranking and differentiation of imaging systems or techniques, is defined[8,27] as:

$$IQF_{inv} = \frac{100}{\sum_{i=1}^{N} C_i \times D_i} \qquad (5)$$

where C_i represents the contrast of the ith plaque cavity at the threshold of visibility, and D_i denotes the corresponding diameter. This figure can serve as a measure for the threshold of visibility contrasts and details, and can be directly employed to compare similar radiological imaging systems or to describe the effects of a change in technique.[28] Thus the higher the IQF_{inv}, the lower the threshold of visibility. The IQF_{inv} was calculated for all analyzed lipid-fibrotic plaque phantom images, resulting in an IQF_{inv} value for each technique (plotted as a function of effective energy.

III. RESULTS

The measured effective energies were 58 KeV (80 kVp) and 69 KeV (120 kVp) for the Philips MDCT, 50 KeV (80 kVp) for the Morita, and 50 KeV (80 kVp) for the Planmeca, respectively, using the reference phantom method previously described. The HVL of the Philips unit at 120 kVp beam was measured to be 9.31 mmAl, and that of the Morita 3D Accuitomo unit 3.34 mmAl using an Unfors Solo detector. The HVL for the Promax at 80 kv was measured to be 2.5 mmAl.

One set of images obtained using each imaging modality for the set of phantoms are presented in Fig. 5 showing axial views of a lipid-fibrotic plaque mixture using a Philips MDCT system at both 80 kVp, 120 kVp, and CBCT images from Morita and Planmeca at 80 kVp. While cast acrylic used in many phantom designs have been reported to be in the 120 ± 4 HU range,[29] the cast acrylic device used in the current experiments were measured to have a mean CT attenuation value of 94.8 ± 2.3 HU, selected for its proximity to that of fibrotic atherosclerotic

tissue.[30-35] The window/levels used for each modality were 345/174, 1498/620, and 700/216 for the Morita, Planmeca, and Philips, respectively. These were kept constant throughout the observation trial for each modality.

   C-D curves were constructed to depict the mutual interdependency and trade-offs of the observable image noise, resolution, contrast, and patient dose. These curves indicate the levels of contrast required for the detection of lesions of different sizes and inherent contrasts, as in the low- and high-density lipid mixtures. Figure 6 shows the resulting C-D curves for 80 and 120 kVp vs. the Morita and Planmeca CBCT units. These curves represent model-predicted C-D diagrams for the same plaque mixtures, resulting from the evaluations of six different observers in the same low-light viewing conditions. As expected, less contrast was required for larger lesion sizes and lower noise levels. Whereas the Planmeca unit yielded a much lower contrast resolution performance among all three scanners, the Morita Accuitomo unit at 80 kVp was visibly sufficient to render distinction between adipose and nonadipose tissues on par with the
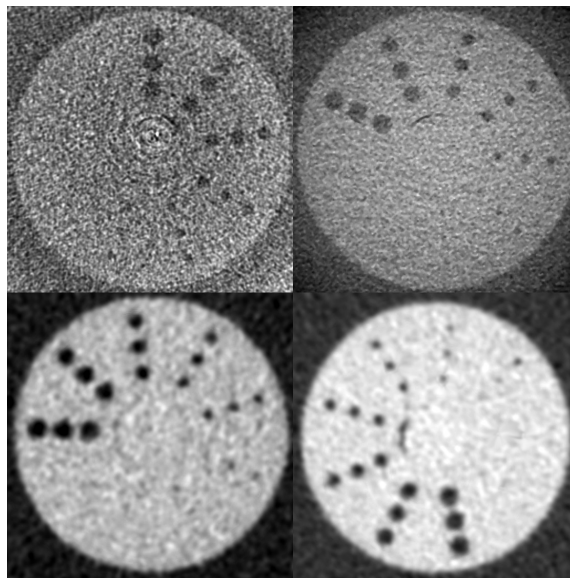

FIG. 5. Axial views of lesion composition phantom as seen from (top-left going clockwise): Planmeca Promax3D (80 kVp), Morita Accuitomo (80 kVp), and Philips MDCT system at 120 kVp and at 80 kVp.
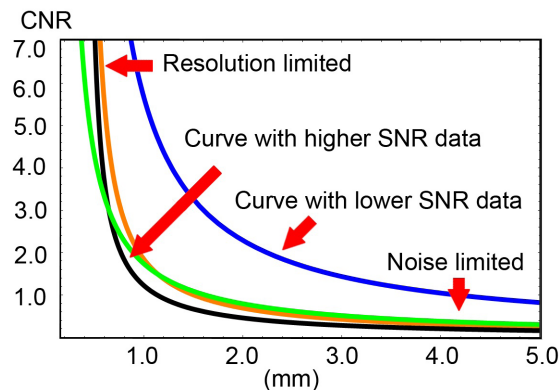

FIG. 6. Interscanner comparison for simulated fibrotic-lipid lesions using Planmeca (blue) at 80 kVp, Morita (green) at 80 kVp, and Philips at 120 kVp (black) and 80 kVp (orange). Each curve relates the size of the minimally perceptible lesion as a function of contrast for different levels of SNR.

clinical 120 kVp Philips protocol images. To quantify this observation, tests of normality were conducted on the observed data which verified that they did not conform to a Gaussian distribution. As a result, the nonparametric Kruskal-Wallis test was used to evaluate all techniques. A significant difference was found for the simulated plaque images of all four techniques (p = 0.037 < 0.05 for Philips at 80 kVp and p = 0.018 < 0.05 for Philips at 120 kVp), indicating that there is a significant difference between the corresponding C-D curves. The Mann-Whitney U test was used to further examine the pair-wise differences between MDCT images obtained at a tube voltage of 80 kVp and those obtained at 120 kVp vs. each CBCT technique. A statistically significant difference was found (p = 0.038 < 0.05 at 80 kVp and p = 0.015 < 0.05 at 120 kVp) between MDCT at 80 kVp and 120 kVp vs. Planmeca C-D curves, while a statistically significant difference was not found between MDCT at 80 kVp and 120 kVp vs. Morita C-D curves (p = 0.878 > 0.05 for Philips 80 kVp and p = 0.382 > 0.05 for Philips at 120 kVp, respectively).

Figure 7 further illustrates the comparison of the four different techniques with a plot of IQF_{inv} as a function of measured effective energy, for each of the six observers. The averaged IQF_{inv}, ordered from highest to lowest, with interobserver variations expressed as standard deviations were 62.63 (± 4.50 SD) for Philips at 120 kVp, 52.28 (± 4.45 SD) for Morita CBCT, 29.60 (± 4.95 SD) for Philips at 80 kVp, and 21.21 (± 2.27 SD) for the Planmeca Promax, respectively.

The phantom CTDI-vol measurements, DLP, as well as estimated effective dose from two detector types are tabulated in Table 2. The CBCT manufacturer displayed a CTDI-vol of 7.9 mGy, which was in close agreement with our measurements. Such was not the case, however, for the MDCT Philips scanner. For example, the manufacturer's displayed CTDI-vol for the 120 kVp protocol on the Philips Brilliance used in this study was 12.9 mGy, which is roughly half the measured value we obtained, indicating that the manufacturer used a 32 cm adult body PMMA phantom to calculate the CTDI-vol. For our protocol, a 16 cm phantom was used as it was more appropriate for determining dose in the neck region. In addition, the effective dose for the Promax model had to be calculated differently, due to an observed asymmetric field. Similar to the method described by Lofthag-Hansen et al.,[36] we calculated the effective dose as the product of the dose area product (DAP) and a conversion factor of 0.08 mSv per Gy cm^2 to arrive at the effective dose of 0.082 mSv for our protocol, which is a lower dose than the other models we examined.
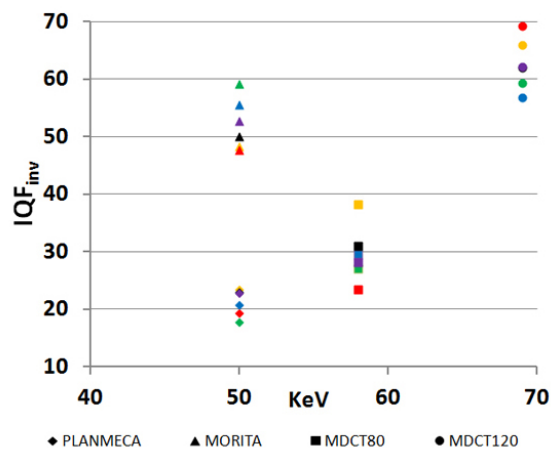

FIG. 7. Individual inverse image quality figure (IQF_{inv}), as described in text, for simulated fibrotic-lipid lesions for all six observers as a function of effective photon energy of the used technique. Planmeca is Promax 3D, Morita is 3D Accuitomo 80 XYZ slice view tomograph, MDCT80 is the Philips Brilliance 64 operating at 80 kVp, and MDCT120 is the Philips Brilliance 64 operating at 120 kVp.

TABLE 2. Dose estimates and measurements.

	Morita 3D Accuitomo	*Philips Brilliance*	*Philips Brilliance*
Type	CBCT	MDCT	MDCT
Tube Potential	80 kVp	120 kVp	120 kVp
Measuring Instrument	Unfors	Unfors	Triad
CTDI-VOL (mGy)	7.49±0.02	24.13±0.11	23.49±0.41
DLP (mGy.cm)	59.94±0.15	193.03±0.84	187.88±3.24
D_{eff}(mSv)	0.35±0.01	1.14±0.01	1.11±0.02

Relative dose measurements obtained from the plaque imaging protocols using OSL detectors for 80 kVp CBCT vs. 120 kVp MDCT also demonstrated a 65% drop in average dose from MDCT to CBCT measurements, which confirmed the drop in effective dose calculated from CTDI measurements.

IV. DISCUSSION

An *in vitro* phantom investigation into soft plaque characterization in which atherosclerotic plaques are simulated with varying size and composition is presented in this study. Scans of the phantoms were obtained using 80 kVp and 120 kVp clinical imaging protocols on an MDCT scanner and a 80 kVp protocol on two CBCT systems. Observer performance C-D curves were computed for five combinations of plaque composition per scan protocol.

While commercial aqueous lipid suspensions in varying proportions have previously been used to produce different lesion compositions for phantoms in similar studies,[37] our plaque composition was based on contents previously reported in the literature to better approximate physiological plaque. Collagen is a major component of the fibrotic cap in advanced lesions, comprising 30% of the dry weight and up to 60%[15] or even 80% of the total protein content of advanced human lesions, with the rest being largely composed of elastin.[16,38] The major collagen type of advanced lesions is the fibrillar collagen type I, accounting for roughly 70% of the total collagen.[15] The percentage composition of phospholipid-free lipids in atheroma have long been identified with the major constituents being free cholesterol (24.3%), free acid glycerides (17.9%), and cholesteryl esters (57.8%) such as oleate, palmitate, and other fatty acid mixtures.[13] Comparison with previously reported CT numbers in lipid-rich[39,40] and fiber-rich[34,39] lesions illustrates that the emulsions used in the present study had attenuation values in the range associated with physiological tissue measurements. While cast acrylic used in CT phantoms has been reported to be in the 120 ± 4 HU range,[29] the cast acrylic used in the current phantom was measured to have a mean CT value of 94.8 ± 2.3 HU, similar to that of fibrotic atherosclerotic tissue.[30-35] Aside from the phantoms and materials used, this study also differs from its predecessors in terms of the analysis method. This study examined extant conventional protocols and their default parameters for imaging soft plaque, such as the Philips Angio neck protocol, rather than seeking to compare the optimal performance capabilities of each system. This approach was used to attain a more realistic comparison of the imaging modalities, and the latter line of inquiry would require a completely different experimental design. Thus the phantoms were imaged with standard clinical imaging scanners using basic conventional protocols (e.g., 120 kVp) rather than a 'best of scanner' customized protocol, in order to determine the observer performance metrics applied to clinical soft plaque imaging.

Another point of distinction was the use of C-D analysis for subjective assessment of image quality, which can be utilized for comparing the diagnostic capabilities of different modalities or one modality under different settings. C-D curves are a well-accepted graphical description of the Hindmarsh-Rose model that describes the threshold contrast for perceiving a target in an image as a function of object (e.g., lesion) detail.[26] Consequently, the relative positions

of the C-D curves would reveal which technique is preferable for generating images that can detect noise-limited targets under poor contrast conditions.[26]

The C-D analysis results in this study highlight the trade-offs in employing clinical CBCT for the case of soft plaque solutions. For example, the Morita C-D curve in Fig. 6 is positioned to the right and adjacent to the MDCT curves. Hence, a lesion of 0.8 mm in diameter would require less contrast to be observed in using the cone-beam unit compared to the MDCT system (assuming that the protocol used in this study was employed). Or, from another perspective, if one is to consider the definition of vulnerable plaque as that of having a large lipid core with at least 40% of its composition being free cholesterol crystals, esters, and other lipids,[41] then according to this same curve for that given percentage (and hence contrast) one can approximate the minimum detectable lesion size for each system. In our specific case, the threshold of visibility for soft plaque solutions is smaller for the Morita cone-beam scanner, given the same level of contrast, and compared with the MDCT protocol, particularly in the submillimeter range. These results are all due to the inherent differences between CBCT and MDCT scanner design. Each manufacturer employs different engineering trade-offs to obtain different desired effects. The reproduced volume, exposure parameters, radiation dose, and distribution vary from CBCT vendor to vendor.[36] For example, the Planmeca Promax unit differs in the method of image acquisition from its Morita counterpart both in terms of beam angle geometry and arc of rotation. The former acquires its images via a 220° arc of rotation and approximately a 15° to 20° projection trajectory, whereas the Morita protocol that we used made a full 360° rotation during exposure and a zero° projection trajectory.

The data presented here suggest that there may be an advantage in terms of contrast resolution to image soft plaque in the carotids at subclinical and clinical kVp using a cone-beam CT. The Morita unit provides an example, producing similar, if not equal, contrast resolution capabilities for viewing plaque solutions compared to a conventional MDCT unit operating at 120 kVp protocol.

The results of this study indicate that additional investigation is required in order to establish the role for plaque detection and characterization using CBCT scanners. In particular, future studies should address the limits of CBCT plaque detection while considering the full range of operating characteristics of these systems.

The present study also identified several issues involved with simulating plaque constituents. These include minimizing sources of variability within the artificial plaque samples including ameliorating partial volume effects inherent in ROI measurements. In addition, it is important to reduce the inhomogeneity of the composed materials (such as the collagen), which cause large fluctuations in the attenuation densities of the *in vitro* plaque. In a similar study performed by Ferencik et al.,[37] gray level densities displayed were affected by the lesion size, as well as composition, which further raises questions for quantifying plaques in a phantom model. Fatty substances are, furthermore, notoriously difficult to manage in submillimeter spaces, especially when mixed with fiber in solution form, which can lead to extensive clumping and regional air bubbles. In addition, a standardized method of performing radiation dose measurements for different CT techniques for purposes of comparison is still lacking.[36]

Nakayama et al.[42] have been able to decrease intrascanner tube voltage and reduce radiation dose at the same time, without any significant image quality degradation. Similarly, Hamann et al.[43] have evaluated and compared the performance of an Infinia Hawkeye 4 SPECT-CT system to a 16 slice diagnostic GE Discovery PET-CT scanner (GE Healthcare, Waukesha, WI), showing a diagnostic advantage of the former in terms of low-contrast detail detection. Although several reports in the literature claim CBCT scanners to emit lower doses of radiation compared to their conventional MDCT counterparts,[36,44,45] a more thorough inquiry into protocol dosimetry must be taken into consideration to better clarify the range of protocols over which these claims are valid. Hence, further study is still required to compare an optimized plaque imaging protocol to conventional MDCT methods.

The current study demonstrated the concept of viewing an atherosclerotic plaque mixture using clinical-grade CBCT systems, operating at tube potentials that are lower than that used for conventional MDCT clinical studies. The relative slight increase in the CT number of the nonadipose soft plaque vs. adipose plaque at lower tube-potential settings might find utility in rendering higher contrast between atheromatous adipose and nonadipose plaques.[26] If one is to attain noise levels comparable to that of standard CT imaging systems, it stands to reason that higher doses would be required.[24] On the other hand, lower energy photons are beneficial in that they should allow for an improved discrimination of soft tissue targets,[46] particularly fat.[24]

V.   CONCLUSIONS

In this study, the design and construction of C-D detectability phantoms for the assessment of the imaging performance of computed tomography for imaging *in vitro* soft plaque solutions are described. These phantoms were used for a series of observer-based measurements on clinical-grade, cone-beam and multiple-row detector CT units, with the results expressed in terms of CNR and Inverted Image Quality Figure. The evidence to the results presented from the CBCT systems studied suggest that a more detailed examination is warranted which would investigate the merits and deficiencies for detecting carotid atherosclerotic plaque with clinical CBCT systems.

ACKNOWLEDGMENTS

REFERENCES

1. Sirineni GK and Stillman AE. Understanding the heart: CT and MRI for coronary heart disease. J Thorac Imag. 2007;22(1):107–13.
2. Detrano R. The case for clinical trials of noninvasive coronary imaging tests. Cleve Clin J Med. 2003;70(8):664–65.
3. Fuster V, Fayad ZA, Badimon JJ. Acute coronary syndromes: biology. Lancet. 1999;353(suppl 2):S5–S9.
4. Tapiovaara MJ and Sandborg M. How should low-contrast detail detectability be measured in fluoroscopy? Med Phys. 2004;31(9):2564–76.
5. Smith RF, Rutt BK, Fox AJ, Rankin RN, Holdsworth DW. Geometric characterization of stenosed human carotid arteries. Acad Radiol. 1996;3(11):898–911.
6. Faulkner K and Moores BM. Contrast-detail assessment of computed tomography scanners. Phys Med Biol. 1986;31(9):993–1003.
7. Hall TJ, Insana MF, Soller NM, Harrison LA. Ultrasound contrast-detail analysis: a preliminary study in human observer performance. Med Phys. 1993;20(1):117–27.
8. De Hauwere A, Bacher K, Smeets P, Verstraete K, Thierens H. Analysis of image quality in digital chest imaging. Radiat Prot Dosimetry. 2005;117(1-3):174–77.
9. Davis SC, Pogue BW, Dehghani H, Paulsen KD. Contrast-detail analysis characterizing diffuse optical fluorescence tomography image reconstruction. J Biomed Opt. 2005;10(5):050501.
10. Suryanarayanan S, Karellas A, Vedantham S, Ved H, Baker SP, D'Orsi CJ.. Flat-panel digital mammography system: contrast-detail comparison between screen-film radiographs and hard-copy images. Radiology. 2002;225(3):801–07.
11. Virmani R, Burke AP, Kolodgie FD, Farb A, Kolodgie FD. Pathology of the Vulnerable Plaque. J Am Coll Cardiol. 2005;47(8s1):C13–C18.
12. Ge J, Chirillo F, Schwedtmann J, et al. Screening of ruptured plaques in patients with coronary artery disease by intravascular ultrasound. Heart. 1999;81(6):621–27.
13. McArthur CS. The acetone-soluble lipoid of the atheromatous aorta. Biochem J. 1942;36(7-9):559–70.

14. Kratky RG, Ivey J, Roach MR. Local changes in collagen content in rabbit aortic atherosclerotic lesions with time. Atherosclerosis. 1999;143(1):7–14.
15. Stary HC, Chandler AB, Dinsmore RE, et al. A definition of advanced types of atherosclerotic lesions and a histological classification of atherosclerosis: a report from the Committee on Vascular Lesions of the Council on Arteriosclerosis, American Heart Association. Circulation. 1995;92(5):1355–74.
16. Libby P. Molecular bases of the acute coronary syndromes. Circulation. 1995;91(11):2844–50.
17. International Electrotechnical Commission. Medical electrical equipment. Vol. IEC publication no. 60601-2-44 Ed. 2.1. Geneva, Switzerland: IEC; 2002.
18. ICRP. Managing patient dose in computed tomography. ICRP Publication 87. Ann. ICRP. 2000;30(4).
19. Mahesh M. MDCT physics: the basics: technology, image quality and radiation dose. Philadelphia: Lippincott Williams & Wilkins; 2009. p.103.
20. McCollough C, Cody D, Edyvean S, et al. The measurement, reporting, and management of radiation dose in computed tomography. AAPM Report No. 96. College Park, MD: AAPM; 2008.
21. Mah P, Reeves TE, McDavid WD. Deriving Hounsfield units using grey levels in cone beam computed tomography. Dentomaxillofac Radiol. 2010;39(6):323–35.
22. Burgess AE and Colborne B. Visual signal detection. IV. Observer inconsistency. JOSA A. 1988;5(4):617–27.
23. Kelsey CA, Moseley RD Jr, Mettler FA Jr, Briscoe DE. Observer Performance as a function of viewing distance. Invest Radiol. 1981;16(5):435–37.
24. Bartling SH, Stiller W, Semmler W, Kiessling, F. Small animal computed tomography imaging. Curr Med Imag Rev. 2007;3(1):45–59.
25. Kalender WA. Computed tomography: fundamentals, system technology, image quality, applications. Erlangen: Publicis; 2011. p.128–130.
26. Hasegawa B. Physics of medical x-ray imaging. Madison, WI: Medical Physics Publishing Corporation; 1987. p.219–234.
27. K. Bacher, P. Smeets, L. Vereecken, et al. Image quality and radiation dose on digital chest imaging: comparison of amorphous silicon and amorphous selenium flat-panel systems. AJR Am J Roentgenol. 2006;187(3):630–37.
28. Thijssen MAO, Thijssen HOM, Merx JL, Lindeijer JM, Bijkerk KR. BIR Report 20: Optimization of image quality and patient exposure in diagnostic radiology. London: BIR; 1989. p.29–34.
29. Sharma DS, Sharma SD, Sanu KK, Saju S, Deshpande DD, Kannan S. Performance evaluation of a dedicated computed tomography scanner used for virtual simulation using in-house fabricated CT phantoms. J Med Phys. 2006;31(1):28–35.
30. Nikolaou K, Becker CR, Muders M, et al. Multidetector-row computed tomography and magnetic resonance imaging of atherosclerotic lesions in human ex vivo coronary arteries. Atherosclerosis. 2004;174(2):243–52.
31. Schroeder S, Kuettner A, Leitritz M, et al. Reliability of differentiating human coronary plaque morphology using contrast-enhanced multislice spiral computed tomography: a comparison with histology. J Comput Assist Tomogr. 2004;28(4):449–54.
32. Schroeder S, Kuettner A, Wojak T, et al. Non-invasive evaluation of atherosclerosis with contrast enhanced 16 slice spiral computed tomography: results of ex vivo investigations. Heart. 2004;90(12):1471–75.
33. Leber AW, Knez A, Becker A, et al. Accuracy of multidetector spiral computed tomography in identifying and differentiating the composition of coronary atherosclerotic plaques. A comparative study with intracoronary ultrasound. J Am Coll Cardiol. 2004;43(7):1241–47.
34. Foster G, Shah H, Sarraf G, Ahmadi N, Budoff M. Detection of noncalcified and mixed plaque by multirow detector computed tomography. Expert Rev Cardiovasc Ther. 2009;7(1):57–64.
35. Viles-Gonzalez JF, Poon M, Sanz J, et al. In vivo 16-slice, multidetector-row computed tomography for the assessment of experimental atherosclerosis. Comparison with magnetic resonance imaging and histopathology. Circulation. 2004;110(11):1467–72.
36. Lofthag-Hansen S, Thilander-Klang A, Ekestubbe A, Helmrot E, Grondahl K. Calculating effective dose on a cone beam computed tomography device: 3D Accuitomo and 3D Accuitomo FPD. Dentomaxillofac Radiol. 2008;37(2):72–79.
37. Ferencik M, Chan RC, Achenbach S, et al. Arterial wall imaging: evaluation with 16-section multidetector CT in blood vessel phantoms and ex vivo coronary arteries. Radiology. 2006;240(3):708–16.
38. Libby P, Geng YJ, Aikawa M, et al. Macrophages and atherosclerotic plaque stability. Curr Opin Lipidol. 1996;7(5):330–35.
39. Kitagawa T, Yamamoto H, Ohhashi N, et al. Comprehensive evaluation of noncalcified coronary plaque characteristics detected using 64-slice computed tomography in patients with proven or suspected coronary artery disease. Am Heart J. 2007;154(6):1191–98.
40. Brodoefel H, Reimann A, Heuschmid M, et al. Characterization of coronary atherosclerosis by dual-source computed tomography and HU-based color mapping: a pilot study. Eur Radiol. 2008;18(11):2466–74.
41. Waksman R, Serruys PW, Schaar J, editors. The vulnerable plaque. London: Informa Healthcare; 2007. p.3–27.
42. Nakayama Y, Awai K, Funama Y, et al. Abdominal CT with low tube voltage: preliminary observations about radiation dose, contrast enhancement, image quality, and noise. Radiology. 2005;237(3):945–51.
43. Hamann M, Aldridge M, Dickson J, Endozo R, Lozhkin K, Hutton BF. Evaluation of a low-dose/slow-rotating SPECT-CT system. Phys Med Biol. 2008;53(10):2495–508.
44. Loubele M, Bogaerts R, Van Dijck E, et al. Comparison between effective radiation dose of CBCT and MSCT scanners for dentomaxillofacial applications. Eur J Radiol. 2009;71(3):461–68.
45. Ludlow JB and Ivanovic M. Comparative dosimetry of dental CBCT devices and 64-slice CT for oral and maxillofacial radiology. Oral Surg Oral Med Oral Pathol Oral Radiol Endod. 2008;106(1):106–14.
46. Ritman E. Micro-computed tomography — current status and developments. Ann Rev Biomed Eng. 2004;6:185–208.